Supplementary Information

Nature-inspired mineralization of wood membrane as sensitive electrochemical sensing device for *in situ* recognition of chiral molecules

Zhenqing Dai, Junli Guo, Tiantian Su, Jinfeng Wang, Zhida Gao* and Yan-Yan Song*

College of Science, Northeastern University, Shenyang 110004, China

*Corresponding author: gaozd@mail.neu.edu.cn; yysong@mail.neu.edu.cn

Table of Contents

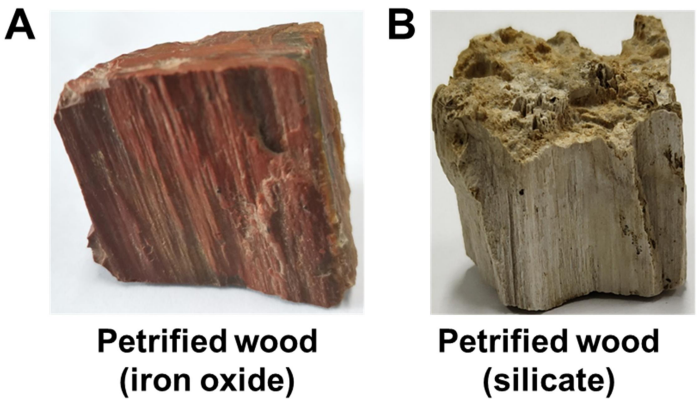

Fig. S1 Digital images of petrified wood.

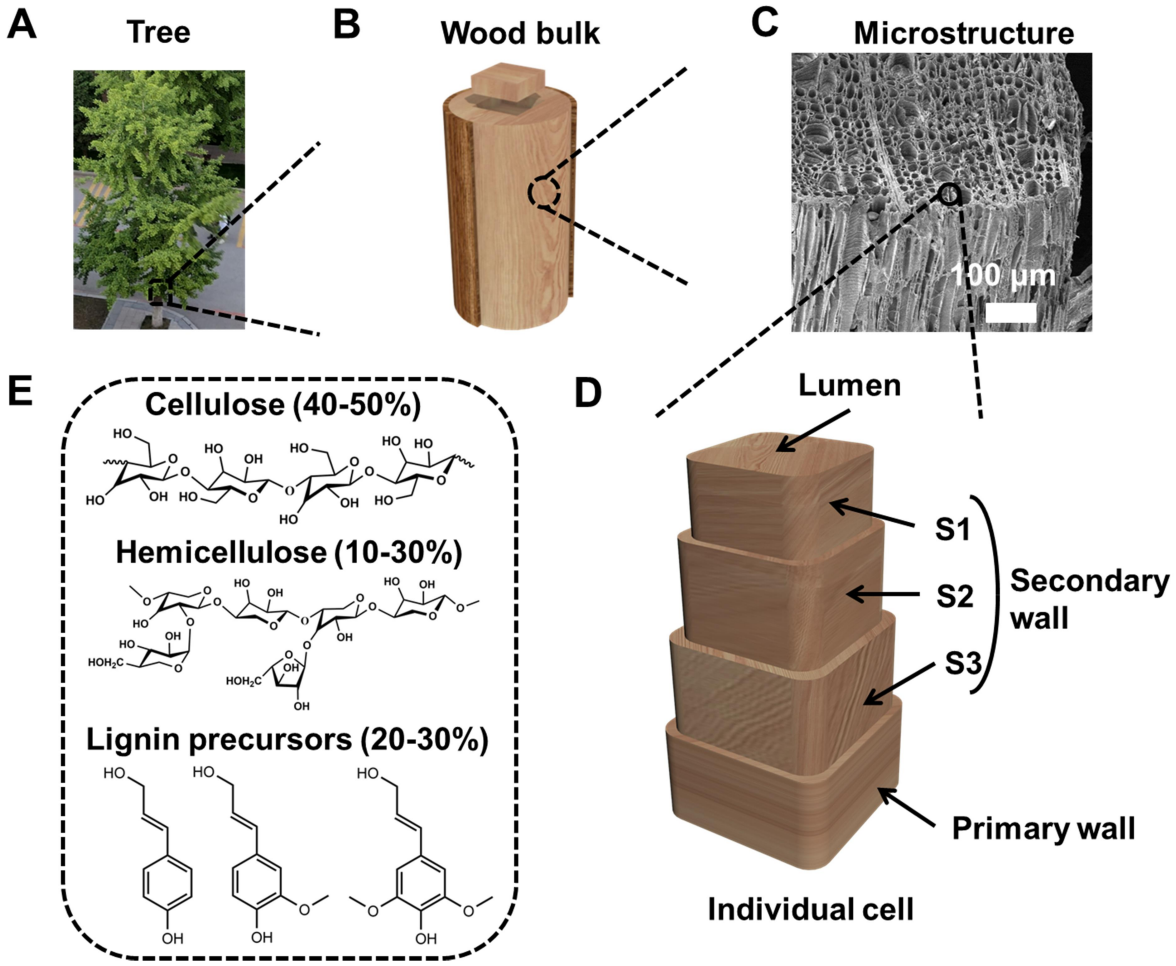

Fig. S2 Graphical illustration of the hierarchical structure of natural wood and the composition of cell wall.

Table S1 Comparison of various cellulosic devices.

Application	Highlights	Reference
Nanofluidic device	*i*) Cationic wood membrane developed for the nanofluidic device. *ii*) Highly conductivity achieved by etherification and densification.	S1
Heat-to-electricity conversion device	*i*) Oxidation of 2,2,6,6-tetramethylpiperidine-1-oxyl (TEMPO) enhanced the negative charge density of the cellulose nanofibers. *ii*) An enhancement effect on thermal-to-voltage conversion achieved on Na–cellulose complex, which was prepared via an electrolyte infiltration.	S2
Versatile sensing devices	*i*) Flexible and breathable electronic devices constructed by using cellulose nanocrystals/iron (III) ion/polyvinyl alcohol composites. *ii*) Good sensing performance in monitoring real-time physical and infection related signals.	S3
Wearable textile sensors	*i*) Conductive silk-polyurethane blended yarns/cellulose nanocrystals-polypyrrole composites applied for multiple signals monitoring. *ii*) Wearable textile sensors assembled by traditional sewing technology with different shapes.	S4
An e-skin device	*i*) Novel cellulose-based dynamic gel constructed by a universal hydrogen-bond topology-regulation strategy. *ii*) Dynamic gel applied for sensing touching, breathing, and sensitive changes in the surrounding environment.	S5
Electrochemical sensing device	*i*) PB-mineralized wood membrane applied for sensitively electrochemical sensing platform. *ii*) Sensing signals effectively amplified by the target activated cascade reactions.	This work

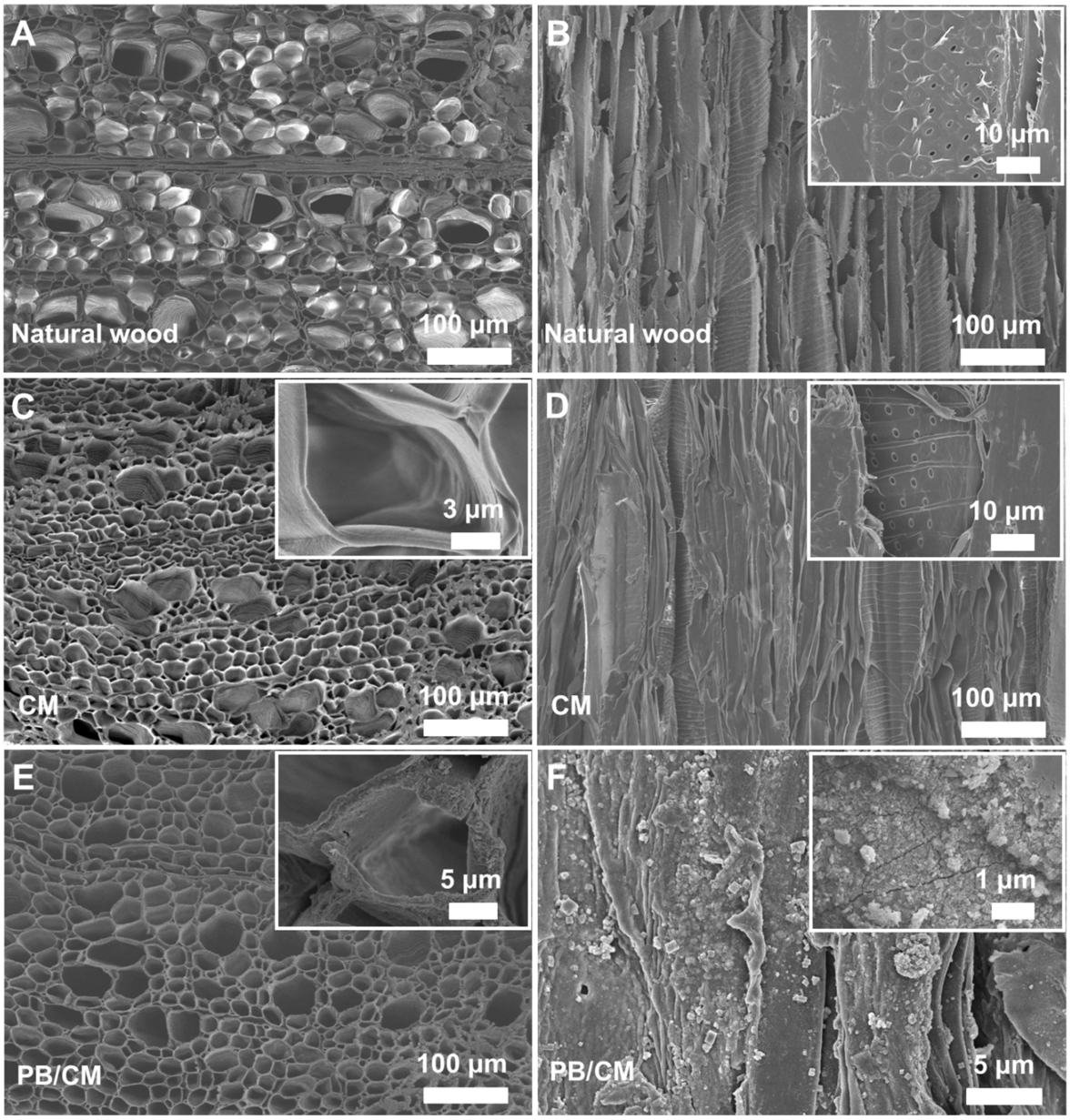

Fig. S3 SEM images of (A) top view and (B) cross-sectional view of natural wood. SEM images of (C) top view and (D) cross-sectional view of CM. SEM images of (E) top view and (F) cross-sectional view of PB-decorated CM. Insets: the corresponding high-magnification SEM images.

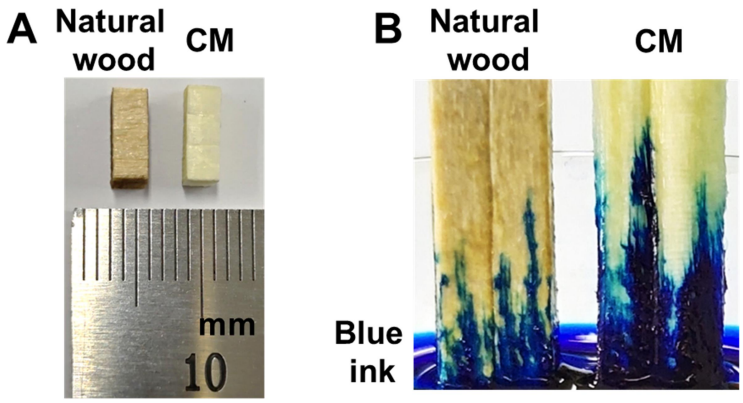

Fig. S4 (A) Digital images of natural wood and CM. (B) Digital images of directional fluidic transport of natural wood and CM.

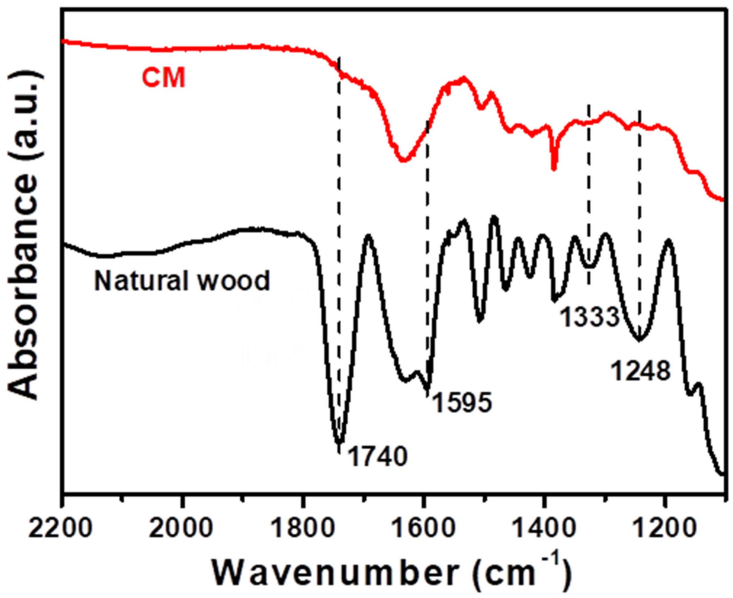

Fig. S5 FT-IR spectra of natural wood and CM.

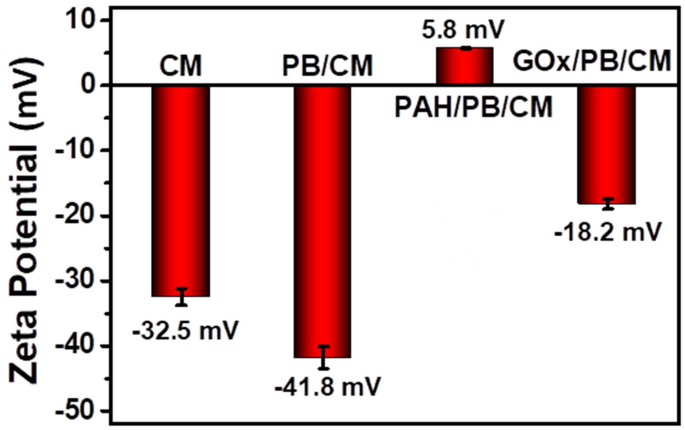

Fig. S6 Zeta potentials of CM, PB/CM, PAH/PB/CM, and GOx/PB/CM. The pH is 6.0 for zeta potential measurements.

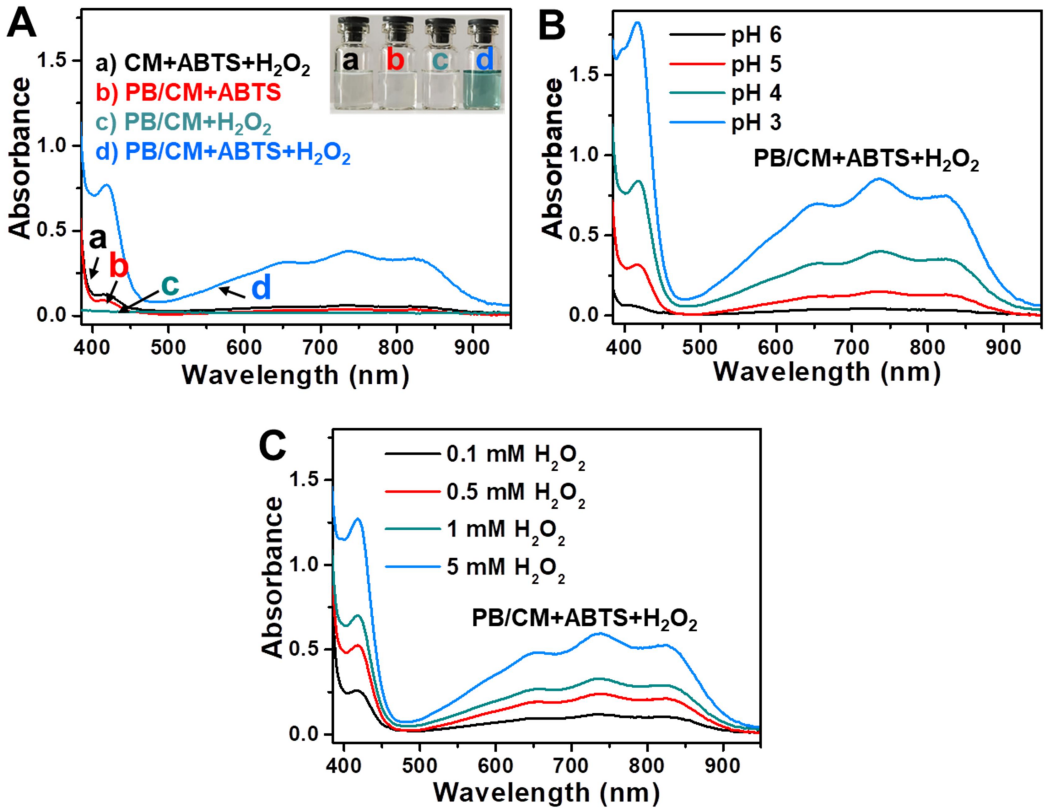

Fig. S7 Colorimetric assay of POD-like reaction of PB. (A) UV−vis spectra of different samples: (a) CM + ABTS + H_2O_2, (b) PB/CM + ABTS, (c) PB/CM + H_2O_2, and (d) PB/CM + ABTS + H_2O_2. Inset images: the corresponding photographs of the solutions corresponding to each curve. POD-like catalytic activity of PB is dependent on (B) pH and (C) H_2O_2 concentration.

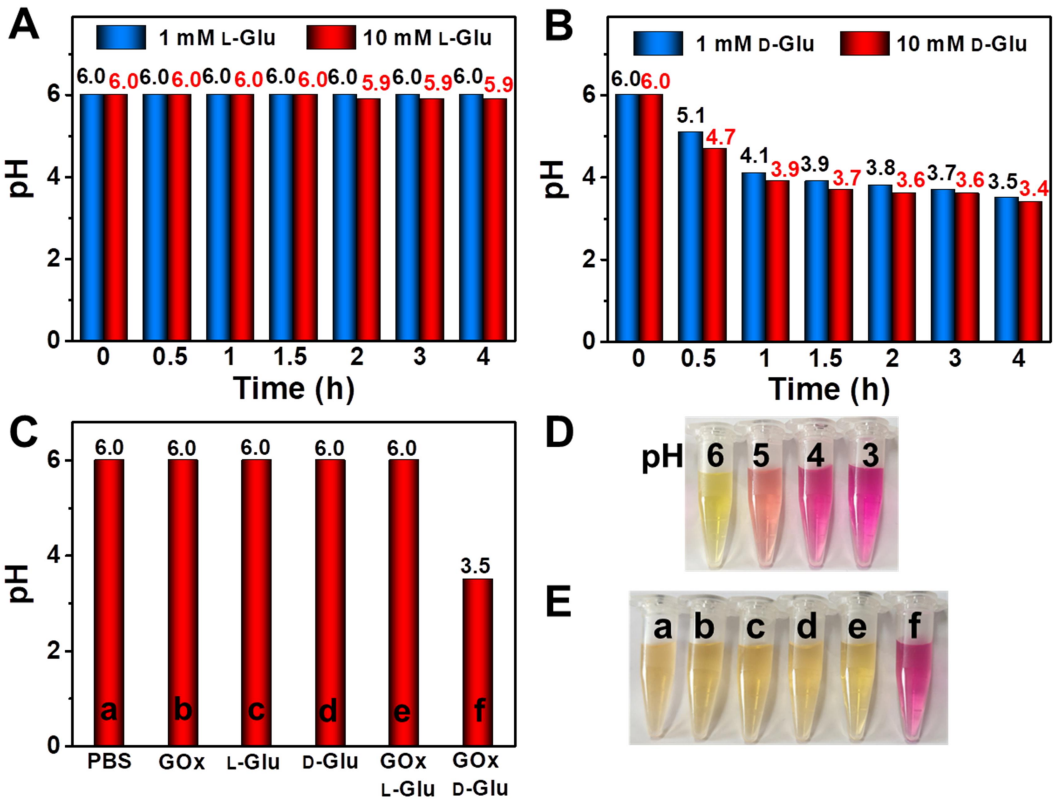

Fig. S8 Variation in pH arising from the reaction between GOx and different concentrations of (A) L-Glu and (B) D-Glu. (C) The pH of different reaction systems in PBS buffer. (D) Standard photographs of phosphate buffers at different pH upon the addition of methyl red. (E) Corresponding photographs of different reaction systems in (C) upon the addition of methyl red.

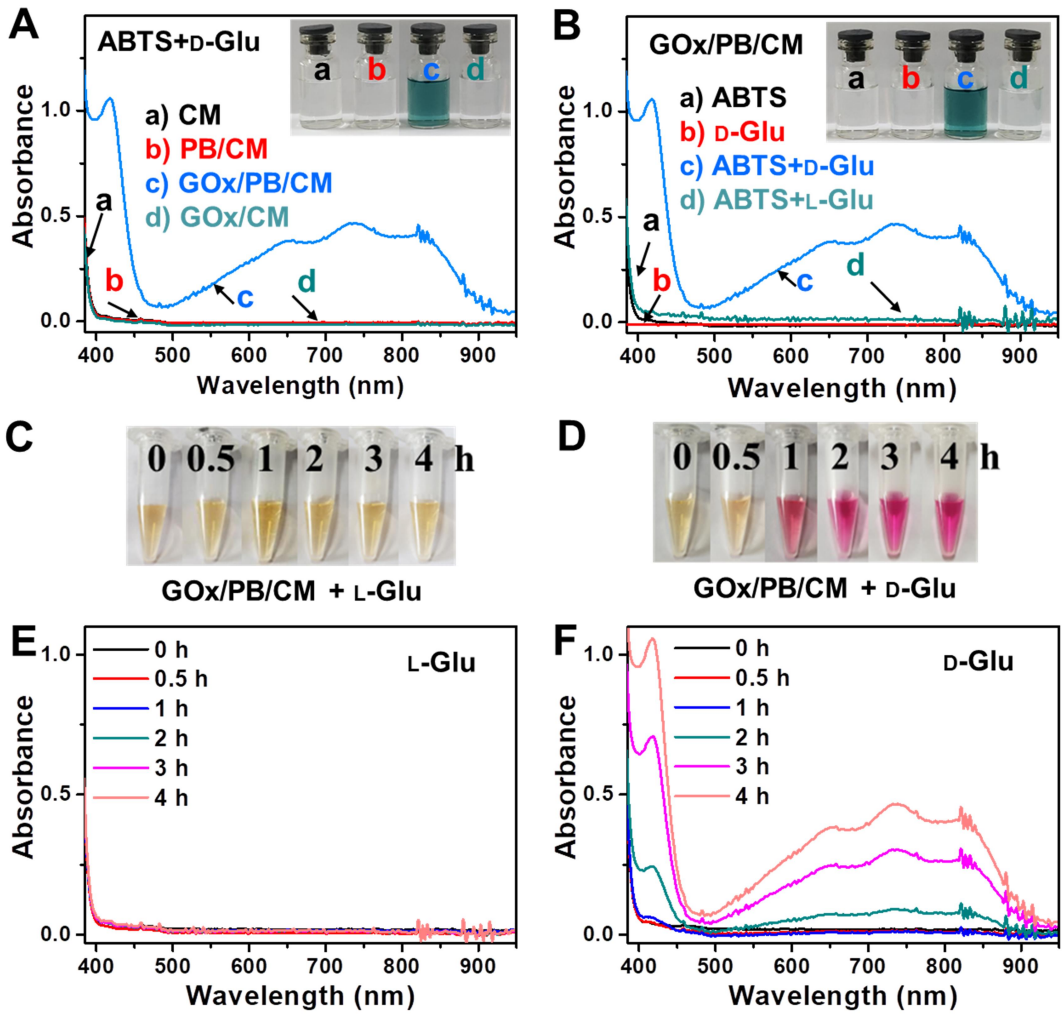

Fig. S9 Colorimetric assay of POD-like activity of PB activated by L/D-Glu. (A) UV−vis spectra of different samples in 1 mM D-Glu, 0.5 mM ABTS, and 0.2 mM PBS buffer solutions: (a) CM, (b) PB/CM, (c) GOx/PB/CM, and (d) GOx/CM. (B) UV−vis spectra of GOx/PB/CM in different solutions: (a) ABTS, (b) D-Glu, (c) ABTS + D-Glu, and (d) ABTS + L-Glu. Inset image: the corresponding photographs of solutions corresponding to each curve. (C and D) Photographs of different reaction systems in 1 mM L/D-Glu and 0.2 mM PBS buffer upon the addition of methyl red. (E and F) UV−vis absorption spectra over time in the presence of 1 mM L/D-Glu, 0.5 mM ABTS, and 0.2 mM PBS (pH 6.0).

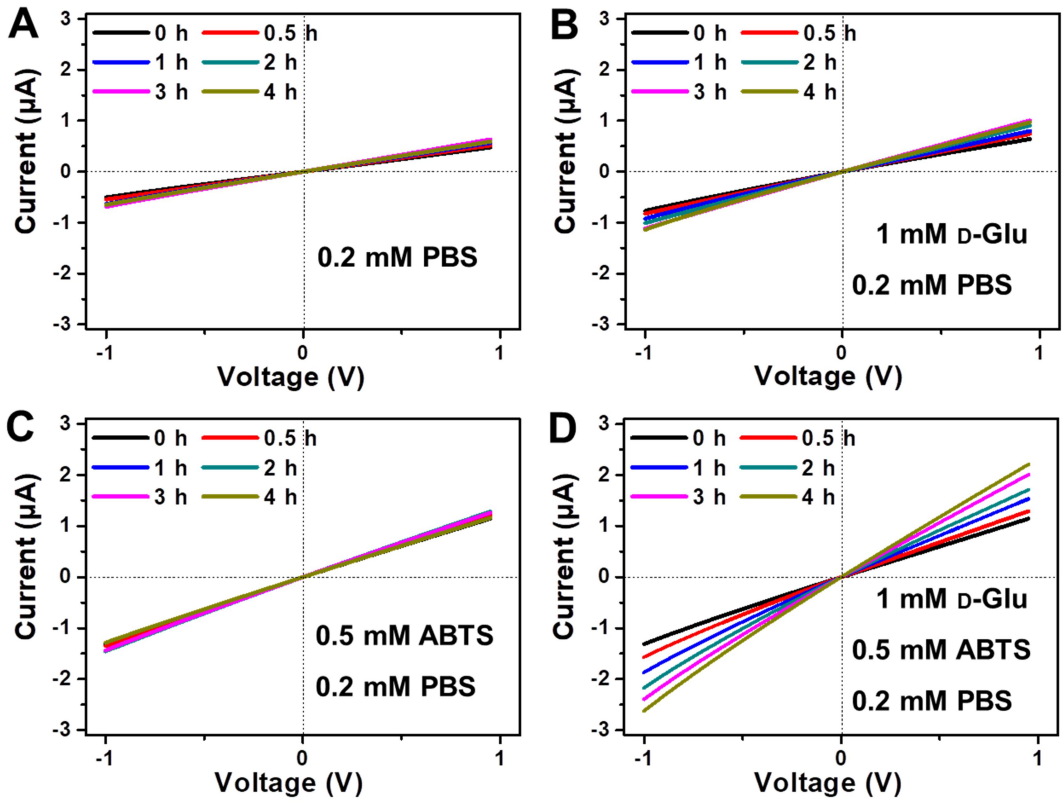

Fig. S10 *I–V* curves for evaluating the POD-like activity in different electrolytes: (A) 0.2 mM PBS buffer, (B) 1 mM D-Glu and 0.2 mM PBS buffer, (C) 0.5 mM ABTS and 0.2 mM PBS buffer, and (D) 1 mM D-Glu, 0.5 mM ABTS, and 0.2 mM PBS buffer.

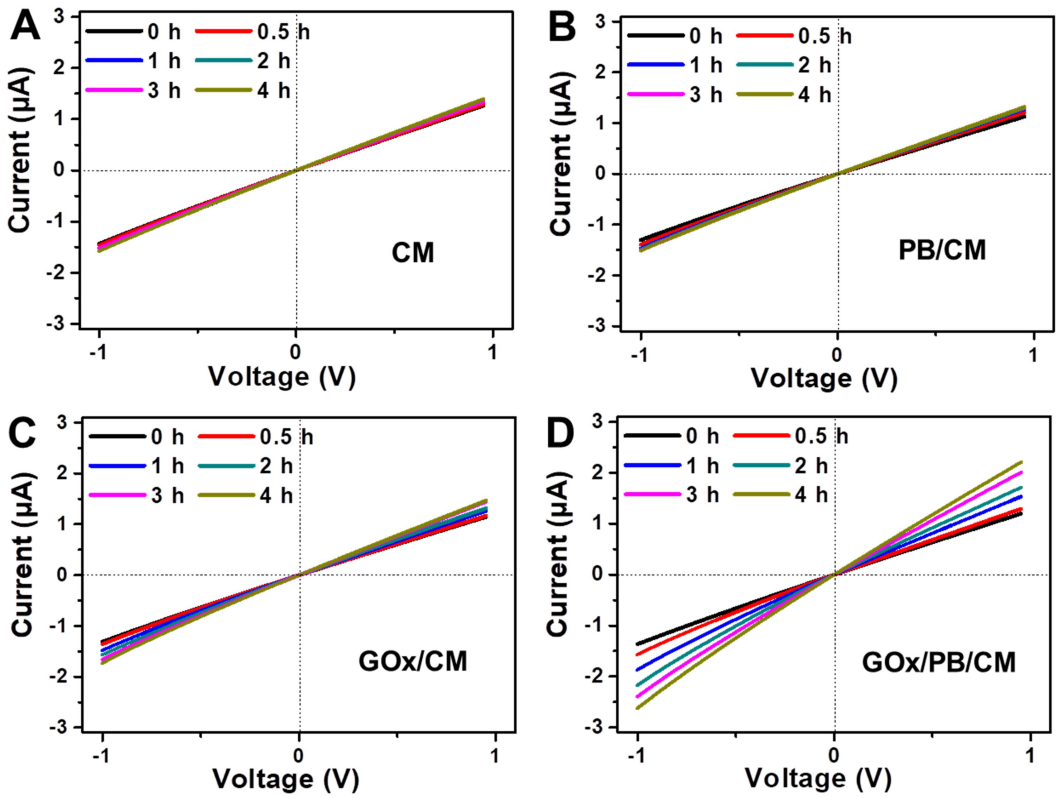

Fig. S11 *I–V* curves for evaluating the effect of membrane composition on POD-like activity: (A) CM, (B) PB/CM, (C) GOx/CM, and (D) GOx/PB/CM. The electrolyte for electrochemical measurement contains 1 mM D-Glu, 0.5 mM ABTS, and 0.2 mM PBS buffer (pH 6.0).

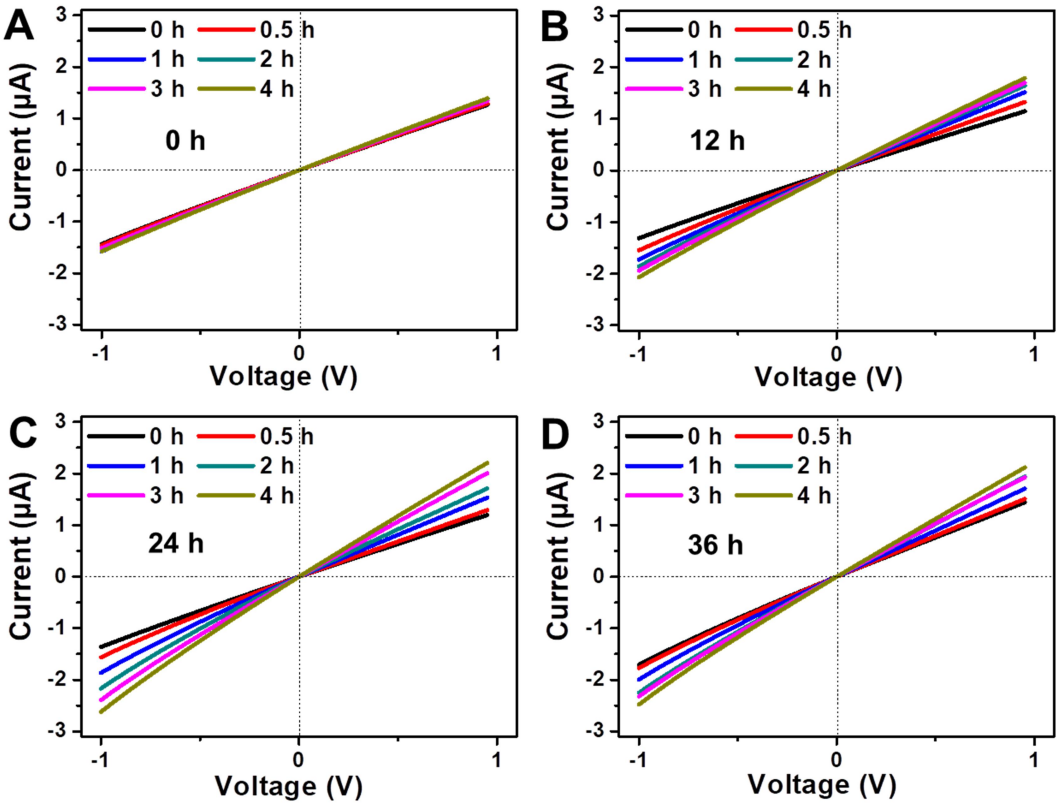

Fig. S12 *I–V* curves for evaluating the effect of the deposition time of PB on the POD-like activity. Electrochemical measurements were performed in an aqueous solution containing 1 mM D-Glu, 0.5 mM ABTS, and 0.2 mM PBS buffer (pH 6.0).

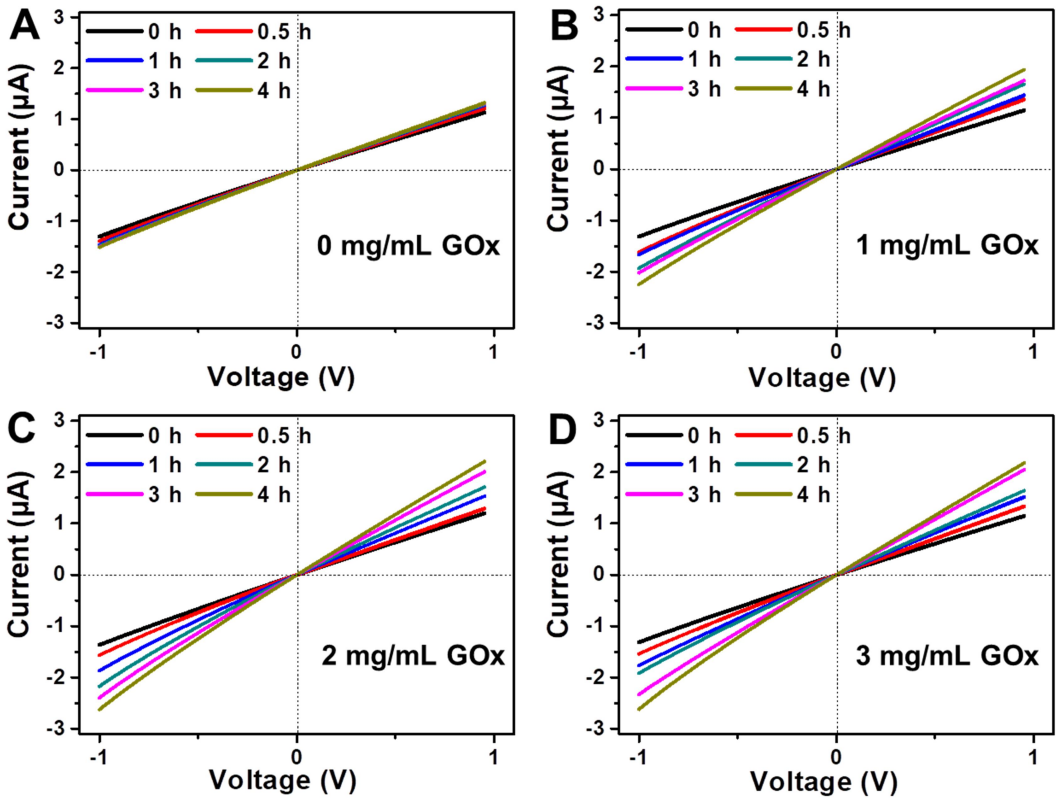

Fig. S13 *I–V* curves for evaluating the effect of GOx concentration on the POD-like activity. Electrochemical measurements were performed in an aqueous solution containing 1 mM D-Glu, 0.5 mM ABTS, and 0.2 mM PBS buffer (pH 6.0).

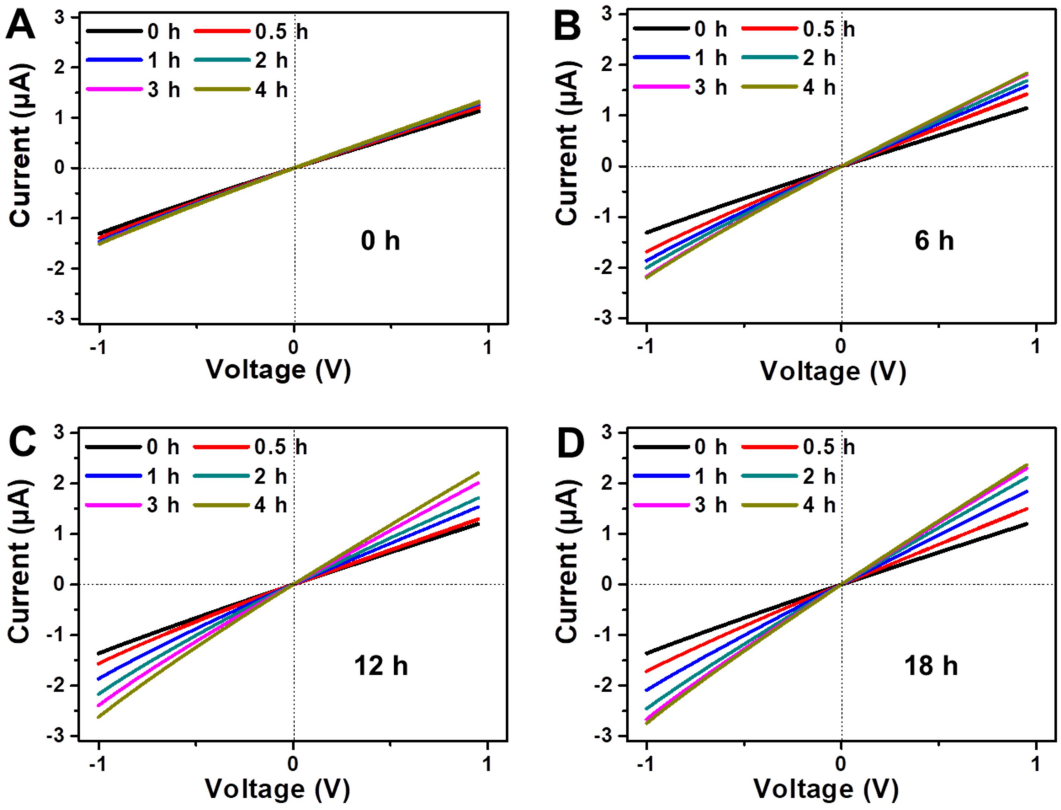

Fig. S14 *I–V* curves for evaluating the effect of GOx assembly time on the POD-like activity. Electrochemical measurements were performed in an aqueous solution containing 1 mM D-Glu, 0.5 mM ABTS, and 0.2 mM PBS buffer (pH 6.0).

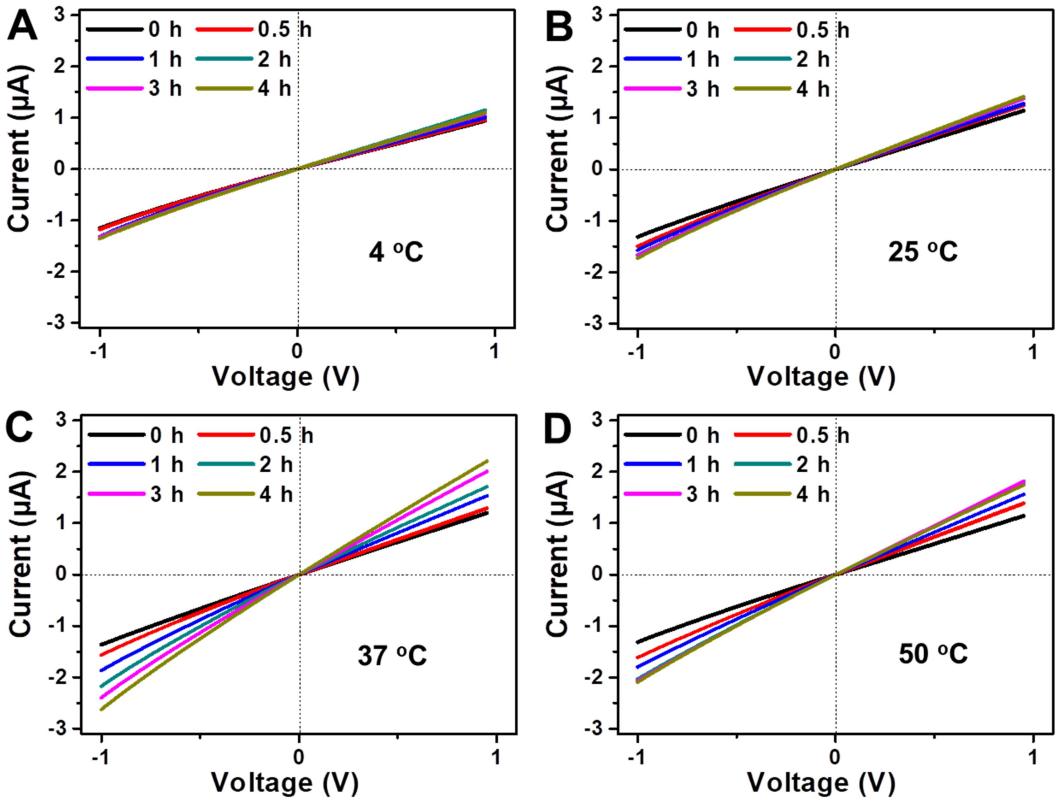

Fig. S15 *I–V* curves for evaluating the effect of incubation time on POD-like activity. Electrochemical measurements were performed in an aqueous solution containing 1 mM D-Glu, 0.5 mM ABTS, and 0.2 mM PBS buffer (pH 6.0).

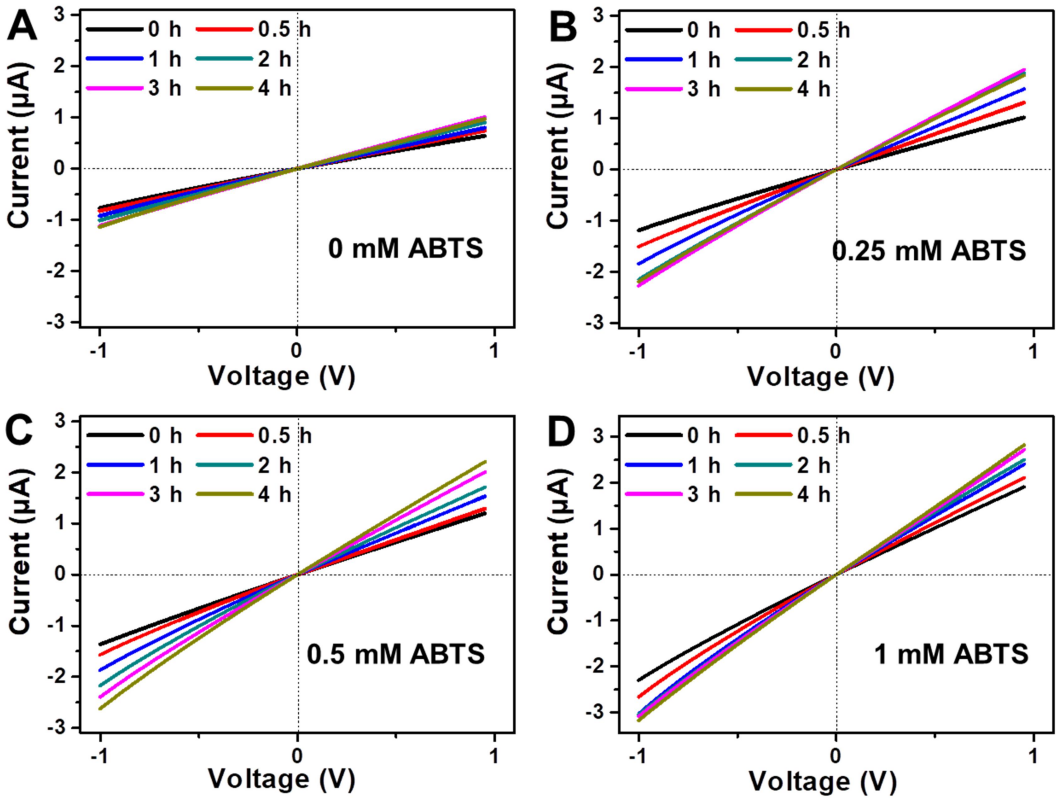

Fig. S16 *I–V* curves for evaluating the effect of ABTS concentration on POD-like activity. Electrochemical measurements were performed in an aqueous solution containing 1 mM D-Glu, 0-1 mM ABTS, and 0.2 mM PBS buffer (pH 6.0).

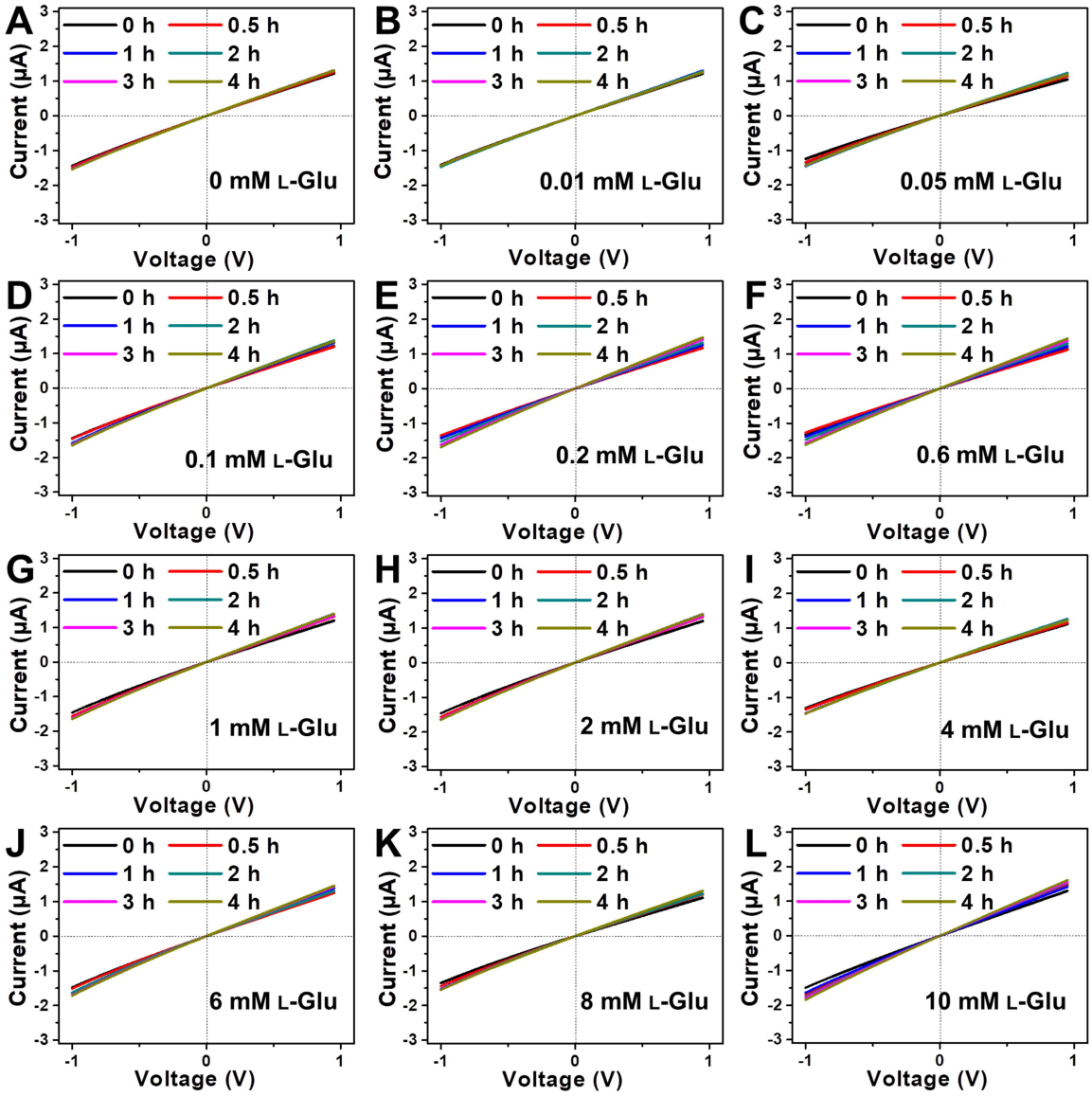

Fig. S17 *I–V* curves for sensing different concentrations of L-Glu. Electrochemical measurements were performed in an aqueous solution containing 0-10 mM L-Glu, 0.5 mM ABTS, and 0.2 mM PBS buffer (pH 6.0).

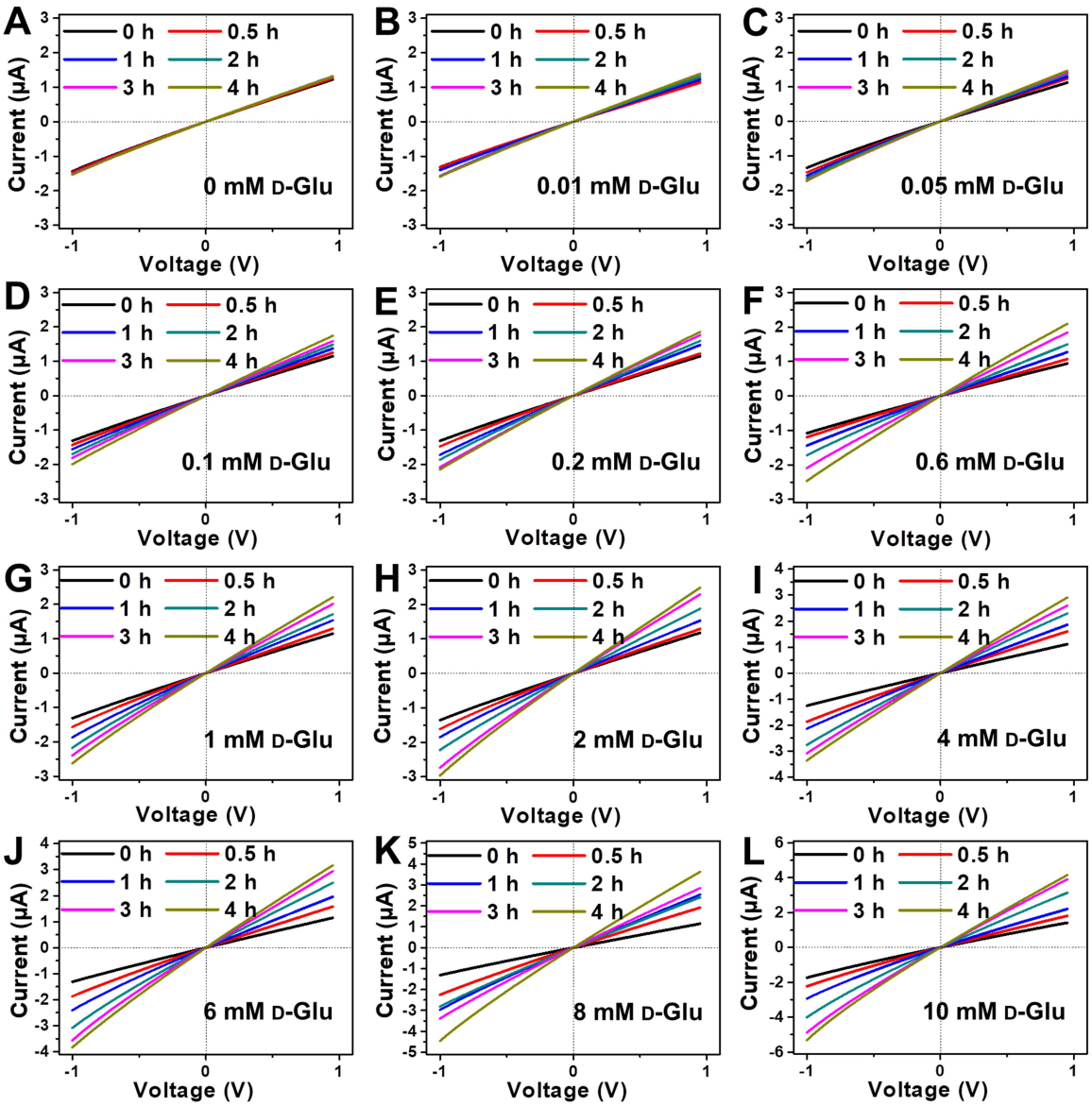

Fig. S18 *I–V* curves for sensing different concentrations of D-Glu. Electrochemical measurements were performed in an aqueous solution containing 0-10 mM D-Glu, 0.5 mM ABTS, and 0.2 mM PBS buffer (pH 6.0).

Table S2 Comparison of various methods for L/D-Glu detection.

Methods	Mechanisms	Sensitivity data	References
Chiral nanochannel-based electrochemical method	The chiral nanochannels modified with a chiral pillar[6]arene-based host–guest system show a high chiral-driven ionic gate for glucose enantiomers.	1 mM	S6
Achiral glucose receptor-based CD assay	Glucose receptor contains bis-ureidobenzenecarboxamido units, which bind to L/D-Glu expected to cause twisting of these chromophores, leading to strong CD signals	40 μM	S7
Gold nanoparticles (AuNPs) with DNA ligands–based colorimetric assay	Random-coiled DNA-capped nanoparticles preferentially catalyze oxidation of L-Glu, and structured DNA-capped nanoparticles show higher activity toward D-Glu	2 mM	S8
Chiral AuNP-based colorimetric strategy	AuNPs modified by polycationic α-cyclodextrin allowed for precise the photocontrol of recognition catalysis for chiral monosaccharides.	100 mM	S9
Self-activated cascade reaction based electrochemical assay	GOx modified in wood channel converts D-Glu (not L-Glu) into gluconic acid and H_2O_2, activating the POD-like activity of PB for further triggering the ionic current response	3 μM	This study

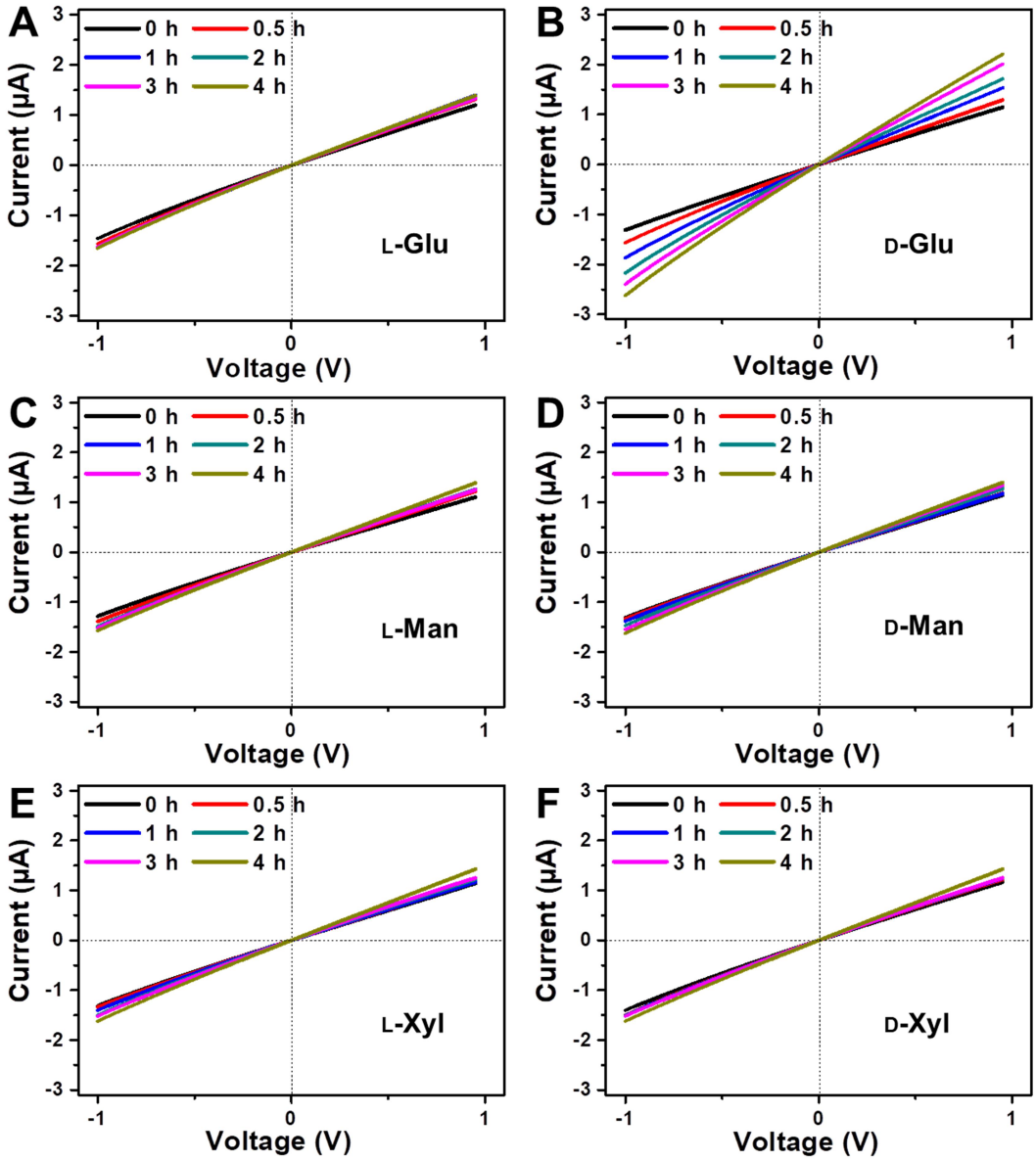

Fig. S19 *I–V* curves for sensing different chiral molecules. Electrochemical measurements were performed in an aqueous solution containing 1 mM L/D-Glu, 1 mM L/D-Man or1 mM L/D-Xyl, 0.5 mM ABTS, and 0.2 mM PBS buffer (pH 6.0).

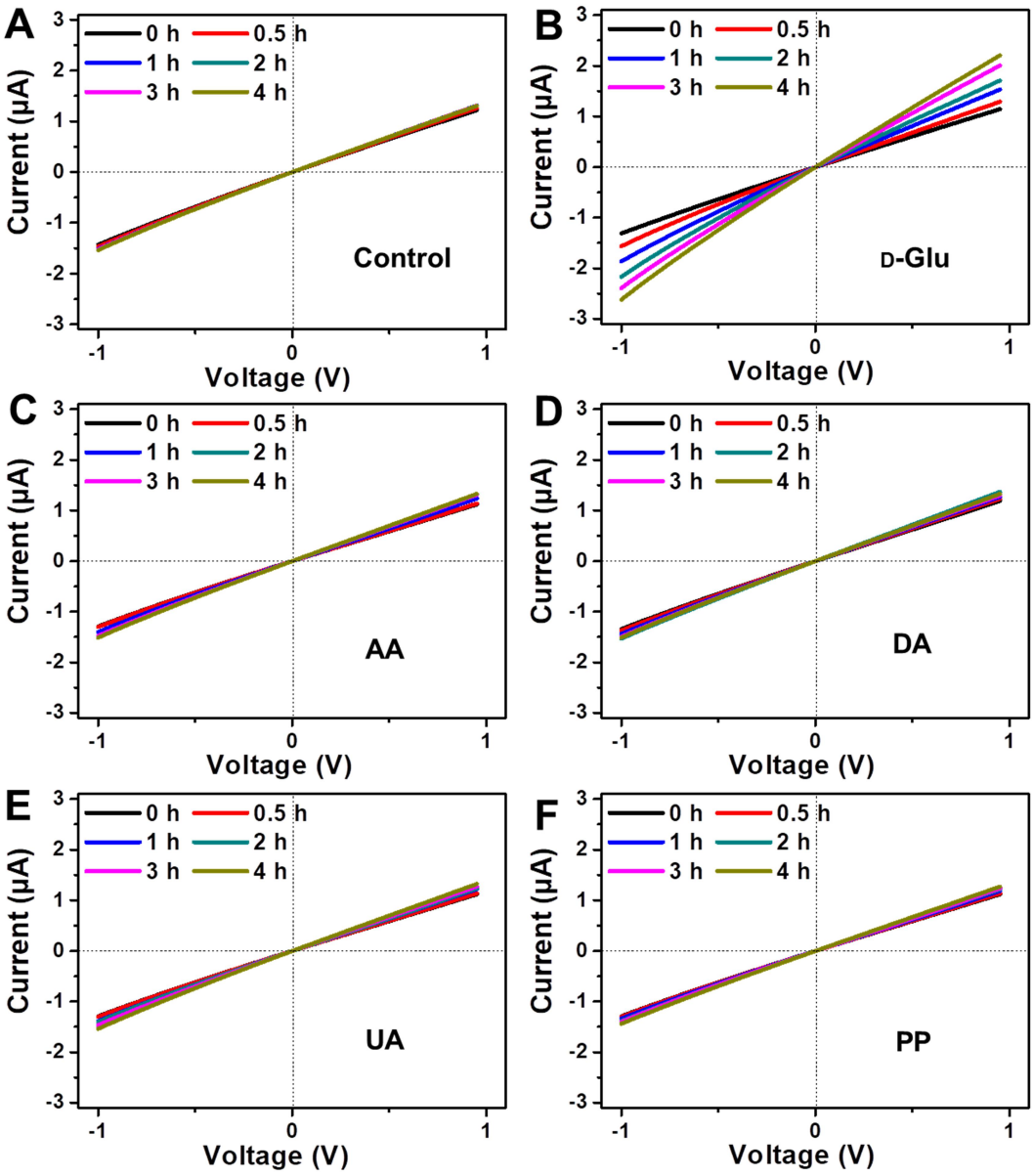

Fig. S20 *I–V* curves for sensing different interfering species. Electrochemical measurements were performed in an aqueous solution containing 1 mM D-Glu, 0.5 mM AA, 0.5 mM DA, 0.5 mM UA or 0.5 mM PP, 0.5 mM ABTS, and 0.2 mM PBS buffer (pH 6.0).

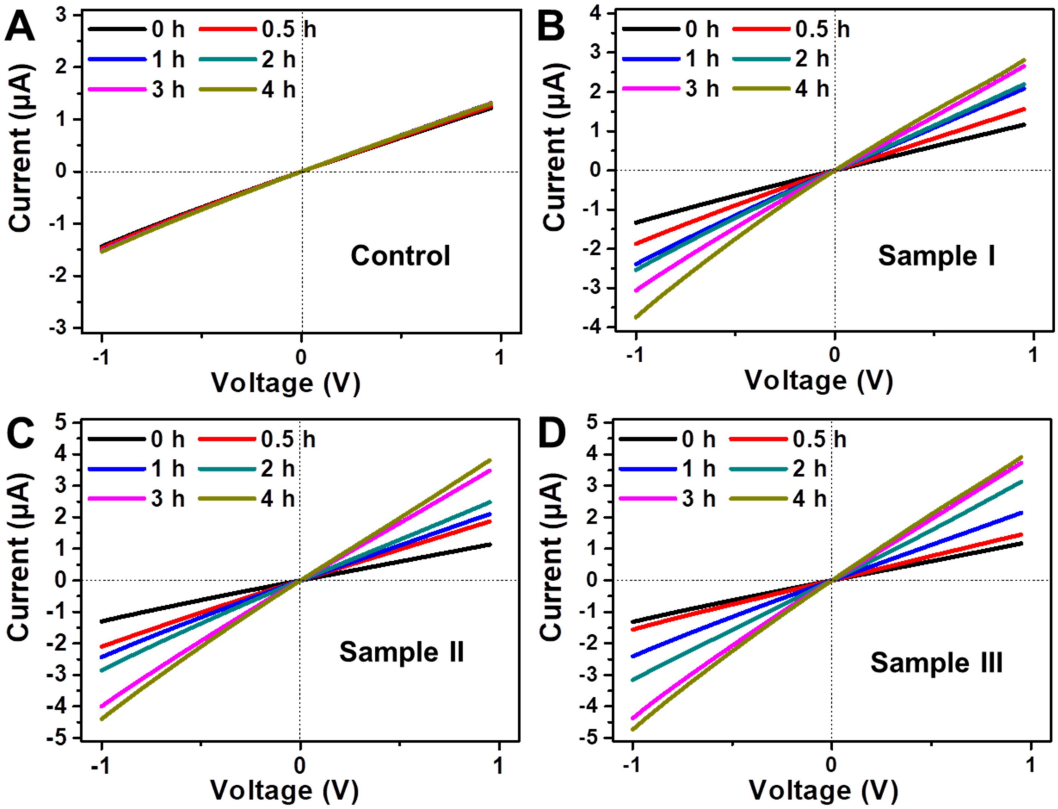

Fig. S21 *I*–*V* curves for sensing D-Glu in serum samples. Electrochemical measurements were performed in an aqueous solution containing 0.5 mM ABTS and 0.2 mM PBS buffer (pH 6.0) in real serum samples.

Table S3 Detection of D-Glu in real serum samples using the proposed method.

Sample	Known concentration (mM)	Detected concentration (mM)	Recovery	RSD
Sample I	5.51	5.63 ± 0.11	102.27%	1.97%
Sample II	8.01	8.16 ± 0.23	101.82%	2.74%
Sample III	9.51	9.51 ± 0.34	99.47%	3.62%

References

S1 G. Chen, T. Li, C. Chen, C. Wang, Y. Liu, W. Kong, D. Liu, B. Jiang, S. He, Y. Kuang and L. Hu, *Adv. Funct. Mater.*, 2019, **29**, 1902772.

S2 T. Li, S. X. Li, W. Kong, C. Chen, E. Hitz, C. Jia, J. Dai, X. Zhang, R. Briber, Z. Siwy, M. Reed and L. Hu, *Sci. Adv.*, 2019, **5**, eaau4238.

S3 Z. Ouyang, S. Cui, H. Yu, D. Xu, C. Wang, D. Tang and K. C. Tam, *Nano Res.*, 2021.

S4 Z. Ouyang, D. Xu, H.-Y. Yu, S. Li, Y. Song and K. C. Tam, *Chem. Eng. J.*, 2022, **428**, 131289.

S5 D. Zhao, Y. Zhu, W. Cheng, G. Xu, Q. Wang, S. Liu, J. Li, C. Chen, H. Yu and L. Hu, *Matter*, 2020, **2**, 390−403.

S6 Y. Sun, F. Zhang, J. Quan, F. Zhu, W. Hong, J. Ma, H. Pang, Y. Sun, D. Tian and H. Li, *Nat. Commun.*, 2018, **9**, 2617

S7 R. A. Tromans, S. K. Samanta, A. M. Chapman and A. P. Davis, *Chem. Sci.*, 2020, **11**, 3223–3227.

S8 P. Zhan, Z-G. Wang, N. Li and B. Ding, *ACS Catal.*, 2015, **5**, 1489−1498.

S9 L. Chen, Y. Chen, Y. Zhang and Y. Liu, *Angew. Chem. Int. Ed.*, 2021, **60**, 7654–7658.